PCCP

ROYAL SOCIETY OF CHEMISTRY

PAPER

View Article Online
View Journal | View Issue

Cite this: *Phys. Chem. Chem. Phys.*, 2025, **27**, 687

A density functional theory study of two-dimensional bismuth selenite: layer-dependent electronic, transport and optical properties with spin–orbit coupling†

Yao Wang, ‡[ab] Jinsen Zhang, ‡[a] Xuanlin Zhang,[d] Chenqiang Hua,*[c] Yunhao Lu[d] and Xinyong Tao [a]

Recently, atomic-thickness van der Waals (vdW) layered bismuth selenite (Bi_2SeO_5) has been successfully synthesized, not only expanding the family of two-dimensional (2D) materials, but also playing a pivotal role in the advancement of 2D electronics as a high-κ dielectric. In this work, we systematically study the basic properties of 2D Bi_2SeO_5 through first-principles calculations, focusing on the spin–orbit coupling (SOC) effect and layer-dependent behaviors. The results show that SOC can adjust the bandgap of bulk/2D Bi_2SeO_5 from direct to indirect, with the bandgap decreasing upon increasing the thickness due to quantum confinement. Importantly, we observe that SOC has a negligible effect on the valence band edge but significantly impacts the conduction band edge, due to the specific distribution of the Bi-p orbital. We also explore the vdW magnetic tunneling junction based on 2D Bi_2SeO_5, which can exhibit significant tunneling magnetoresistance between the parallel and antiparallel magnetic alignments of electrodes, *e.g.* 900% for 1L and 1800% for 2L. As for the optical properties, strong layer dependence is also verified, and the large absorption coefficient is determined to be $\sim 10^6$ cm^{-1}. At last, we also explore the piezoelectric properties. Overall, layered Bi_2SeO_5 is a potential candidate material for electronic device and optoelectronic applications, as well as nano-spintronic applications.

Received 1st October 2024,
Accepted 2nd December 2024

DOI: 10.1039/d4cp03782k

rsc.li/pccp

1. Introduction

Spin–orbit coupling (SOC), a fundamental quantum mechanical interaction between the spin and orbital angular momentums, plays a pivotal role in determining the electronic structure, optical properties, and transport phenomena in materials.[1–4] Specifically, SOC can induce profound modifications in band structures, manifesting as phenomena such as spin splitting, spin scattering and band inversion, *etc.*,[5–7] rendering materials with strong SOC particularly promising for next-generation optoelectronic, spintronic, and quantum computing applications.[8,9] Van der Waals (vdW) layered materials have emerged as a revolutionary platform for materials science research in recent decades.[10–14] A distinctive advantage of vdW materials lies in their atomically precise surfaces characterized by the absence of dangling bonds, exceptional thickness uniformity, and atomically smooth interfaces-properties that markedly distinguish them from conventional three-dimensional materials.[15] Remarkably, vdW systems always show the layer-dependent properties when the thickness is confined to sub-nanometer (few-layer). The interplay between SOC and quantum confinement effects in ultrathin vdW materials offers unprecedented opportunities to engineer their electronic structure and transport properties with atomic-layer precision, which establishes a versatile platform for designing next-generation multifunctional materials with precisely tailored properties, enabling transformative advances in quantum technology, optoelectronics, and spintronics.[16–18]

Very recently, large-scale two-dimensional (2D) bismuth selenite (Bi_2SeO_5) with a high dielectric constant has been achieved through layer-by-layer oxidation or exfoliation.[19–21] Layered Bi_2SeO_5 was reported to have a large bandgap and as a high-κ dielectric, it can show improved electronic performance compared to 2D materials such as Bi_2O_2Se, MoS_2, and graphene due to suppression of the current leakage.[22] SOC

[a] *College of Materials Science and Engineering, Zhejiang University of Technology, Hangzhou 310014, China. E-mail: wangyao@zjut.edu.cn, 2112025100@zjut.edu.cn, tao@zjut.edu.cn*
[b] *Moganshan Research Institute at Deqing County Zhejiang University of Technology, Huzhou 313000, China*
[c] *Hangzhou International Innovation Institute, Beihang University, Hangzhou 311115, China. E-mail: huachenqiang@buaa.edu.cn*
[d] *School of Physics, Zhejiang University, Hangzhou 310027, China. E-mail: 11926054@zju.edu.cn, luyh@zju.edu.cn*

† Electronic supplementary information (ESI) available. See DOI: https://doi.org/10.1039/d4cp03782k

‡ Yao Wang and Jinsen Zhang contributed equally to this work.

plays a pivotal role in the electronic structure, and thus, it may be important for Bi-based system. In addition, as a vdW material, the layer-dependent properties have not been studied yet, including the electronic, transport, optical, and piezoelectric properties, *etc.* Therefore, an in-depth study is necessary.

In this paper, the geometric, electronic, transport, optical, and piezoelectric properties of bulk/2D Bi_2SeO_5 are investigated using density functional theory (DFT). The cleavage energy is 31.87 meV Å^{-2}, indicating the experimental exfoliation feasibility. The band calculations exhibit that the bandgap decreases from 3.06 to 2.79 eV with an exponential tendency, and SOC will further reduce the bandgap by $\sim$0.3 eV. Interestingly, it is found that the valence band (VB) edge is dominated by the O-p orbital, and Bi-p contributes obviously to the conduction band (CB) edge. As a result, SOC mainly affects the CBs while leaves the VBs intact, which is quite different from the normal metal compounds. Next, we construct a vdW $FeS_2/Bi_2SeO_5/FeS_2$ magnetic tunneling junction (MTJ) and it shows significant tunneling magnetoresistance (TMR). The optical properties of 2D Bi_2SeO_5 show obvious layer dependence and SOC modulation, and large absorption coefficients ($\sim 10^6$ cm^{-1}) are also observed. Finally, we show that bulk/2D Bi_2SeO_5 has broken inversion symmetry, and possibly has potential for piezoelectric applications. Our study not only reveals that SOC is both intriguing and significant for Bi_2SeO_5, but also highlights the layer-dependent electronic, optical, and piezoelectric properties of 2D Bi_2SeO_5, emphasizing its potential applications in spintronics.

2. Computational methods

We performed first-principles calculations using the Vienna *Ab initio* Simulation Package (VASP) to describe the exchange–correlation potential by the generalized gradient approximation (GGA) of Perdew–Burke–Ernzerhof (PBE).[23–25] The interactions between the nuclear and valence electrons were described by the projected augmented wave (PAW) potential, with an energy-cutoff of 520 eV for the plane-wave basis. A $3 \times 2 \times 6/2 \times 6 \times 1$ *k*-point mesh was used to sample the Brillouin zone (BZ) of primitive bulk/2D Bi_2SeO_5. To avoid the interactions between the periodic images perpendicular to the basal plane, we included a vacuum space of 20 Å. We tested different vdW interactions and chose the optB86b exchange functional (optB86b-vdW).[26] The systems were optimized with a force threshold of 10^{-3} eV Å^{-1} and the energy convergence criterion was set to be 10^{-6} eV. SOC was included due to the heavy element Bi.[27] A hybrid-exchange functional (HSE06)[28] with the PBE functional was used to compare the band structure.

In order to obtain more information about the transport properties of 2D Bi_2SeO_5, we investigated its relaxation time (τ) based on the Bardeen–Shockley deformation potential (DP) theory for 2D materials:[29,30]

$$\tau = \frac{\mu m^*}{e} = \frac{2\hbar^3 C}{3k_B T m^* {E_1}^2}, \quad (1)$$

where m^*, $\hbar$, k_B, C, T and E_1 are the effective mass, Planck constant, Boltzmann constant, elastic constant, temperature and DP constant, respectively.

We used double-zeta polarization function (DZP) to initialize the Kohn–Sham states and adopted the nonequilibrium Green's function (NEGF-DFT) to calculate the transmission properties. The corresponding energy cutoff was set to be 80 Hartee. Then, the *k*-point meshes of the scattering region and the electrode were set to $4 \times 11 \times 1$ and $4 \times 11 \times 100$, respectively. The energy convergence criteria for both self-consistent calculations and transmission spectrum calculations were consistently set to 10^{-5} eV. Transmission spectra were calculated using Nanodcal[31] and Atomistic ToolKit[32,33] software.

The linear optical properties can be derived from its complex dielectric function, providing crucial insights into its applicability in advanced optoelectronic technologies:

$$\varepsilon(\omega) = \varepsilon_1(\omega) + i\varepsilon_2(\omega), \quad (2)$$

where ω represents the photon frequency. The imaginary part $\varepsilon_2(\omega)$ can be computed from the momentum matrix elements, while the real part $\varepsilon_1(\omega)$ can be derived from $\varepsilon_2(\omega)$ utilizing the Kramer–Kronig relationship:

$$\varepsilon_1(\omega) = 1 + \frac{2}{\pi} p \int_0^\infty \frac{\Omega \varepsilon_2(\omega)}{\Omega^2 - \omega^2} d\Omega, \quad (3)$$

where p is the principal value of integral. The refractive spectrum $n(\omega)$ and optical absorption coefficients $\alpha(\omega)$ are calculated using the formula:

$$n(\omega) = \left(\frac{\sqrt{{\varepsilon_1}^2 + {\varepsilon_2}^2} + \varepsilon_1}{2} \right)^{1/2}, \quad (4)$$

$$\alpha(\omega) = \left(\sqrt{2}\omega \left[\sqrt{\varepsilon_1(\omega)^2 + \varepsilon_2(\omega)^2} - \varepsilon_1(\omega) \right]^{\frac{1}{2}} \right). \quad (5)$$

3. Results and discussion

3.1 Geometric and electronic properties of bulk/2D Bi_2SeO_5

3.1.1 Bulk Bi_2SeO_5. Firstly, bulk Bi_2SeO_5 is studied as depicted in Fig. 1a. Bulk Bi_2SeO_5 belongs to the orthogonal lattice with a space group of *ABM*2. Along the *c*-direction, covalently saturated Bi_2SeO_5 layers are AA-stacked, reflecting the vdW gap between layers. To study the vdW interactions, we utilize different vdW methods to optimize the bulk structure and then compare the lattice constants with experimental ones.[19,21,34] The corresponding results are summarized in Table S1 (ESI†). As shown in Table 1, Tables S1 and S2 (ESI†), we find that DFT-D3,[35] dDsC,[36,37] optB88-vdW,[38] optB86b-vdW,[26] and rev-vdW-DF2[39] methods can yield better results than others, *e.g.*, relative differences are within 1%. We finally adopt the optB86b-vdW functional, since it gives the smallest variation of the volume[19,21,34] and the corresponding lattice constants are a = 11.33, b = 16.37, and c = 5.52 Å, respectively.

As shown in Fig. 1b, we find that bulk Bi_2SeO_5 is a semiconductor with a direct bandgap of 2.79 eV at the Z point,

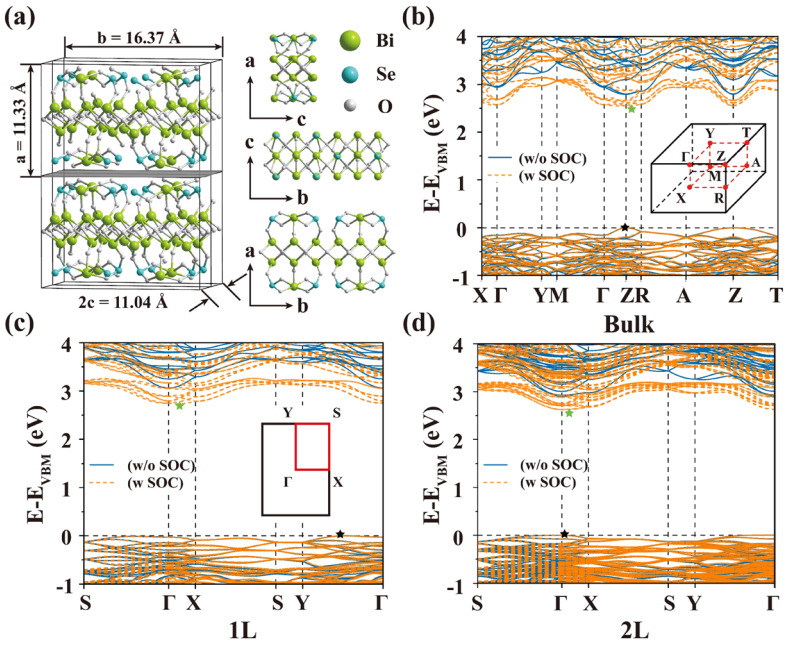

Fig. 1 (a) Crystal structure of bulk Bi_2SeO_5. The vdW gap is marked with a gray plane, reflecting the cleavage position. Electronic band structures of (b) bulk, (c) 1L and (d) 2L Bi_2SeO_5 with SOC (orange dashed lines). For easy comparison, we plot the bands without SOC together (blue solid lines). Green and black pentagrams represent the CBM and VBM, respectively. Inset: The Brillouin zones of (b) bulk and (c) 2D Bi_2SeO_5 with high symmetry points and lines.

Table 1 Lattice constants and the volume of bulk Bi_2SeO_5 calculated by using different computational methods

System	a (Å)	b (Å)	c (Å)	V (Å^3)
Exp.	11.44	16.28	5.49	1022.48
DFT-D3BJ	11.37	16.41	5.52	1029.93
dDsC	11.38	16.43	5.52	1032.09
optB88-vdW	11.37	16.44	5.54	1035.55
optB86b-vdW	11.33	16.37	5.52	1023.81
rev-vdW-DF2	11.35	16.40	5.53	1029.35

which is consistent with the previous calculations[21] and also suitable for ultraviolet optoelectronic devices.[40,41] We also use the HSE06 functional to compare the band structure, which also has a direct bandgap (of 3.87 eV), as shown in Fig. S1a (ESI†). Near the conduction band minimum (CBM) and valence band maximum (VBM), *i.e.* the Z point, the effective mass is calculated to be 0.397 m_0 [electron effective mass (m_e)]/5.345 m_0 [hole effective mass (m_h)] along the Z–T direction, reflecting that the top VB is weakly dispersed (see Fig. 1b). Here m_0 represents the electron mass. In addition, the calculated values of effective mass are 1.431 m_0 (m_e)/0.998 m_0 (m_h) along the Z–Γ direction, and 0.776 m_0 (m_e)/1.580 m_0 (m_h) along the Z–R direction, respectively. These results are comparable to those of some typical 2D materials, such as MoS_2 (0.48 m_0)[42] and h-BN (0.99 m_0).[43]

We also plot the local density of states (LDOS) in Fig. 2a. It is found that the VBs are dominated by the O-p orbital, and the contribution of the Bi-p orbital becomes the largest near the CBM. Such a behavior is different from that of normal metal compounds, in which the s orbital of the metal is not negligible near the CBM.[44] In Fig. 2a, we present a detailed plot of the partial density of states (PDOS), revealing that the p_y and p_z orbitals of Bi have nearly equal contribution, both of which are significantly larger than the Bi-p_x orbital. This suggests that the interlayer interaction in this compound effectively mixes the out-of-plane and in-plane orbitals [see the spatial distribution of wavefunction for the lowest CBs in Fig. S2a–c (ESI†)].

3.1.2 Two-dimensional Bi_2SeO_5. The exfoliation energy is firstly estimated using the equation below:[45]

$$E = \frac{E_{\text{Bulk}} - E_{\text{1L}}}{A}, \tag{6}$$

where E_{Bulk} and E_{1L} denote the energy of the optimized bulk and 1L Bi_2SeO_5; A is the area of the basal plane. The calculated exfoliation energy is 31.87 meV Å^{-2}, which is comparable to 28.35 meV Å^{-2} (h-BN)[46] and ~21 meV Å^{-2} (MoS_2).[45] Thus, we believe bulk Bi_2SeO_5 can be exfoliated to the 2D form. Indeed, previous experiments have successfully exfoliated 2D Bi_2SeO_5.[22]

Typically, the thickness has a significant influence on the basic properties of layered systems due to the quantum confinement.[47] For instance, single-layer MoS_2/$MoSe_2$ has a direct bandgap while multilayer systems have indirect bandgaps.[48,49] Therefore, we further investigate the layer-dependent electronic properties of 2D Bi_2SeO_5, and several results are summarized in Table 2. For example, the in-plane lattice constants gradually increase by 0.04 Å when reducing the thickness from the bulk to 1L Bi_2SeO_5, which can be ascribed to the decreased interlayer interaction. The bandgap variation under the quantum confinement effect is also discussed and verified [see Note S1 and Fig. S3 (ESI†)].

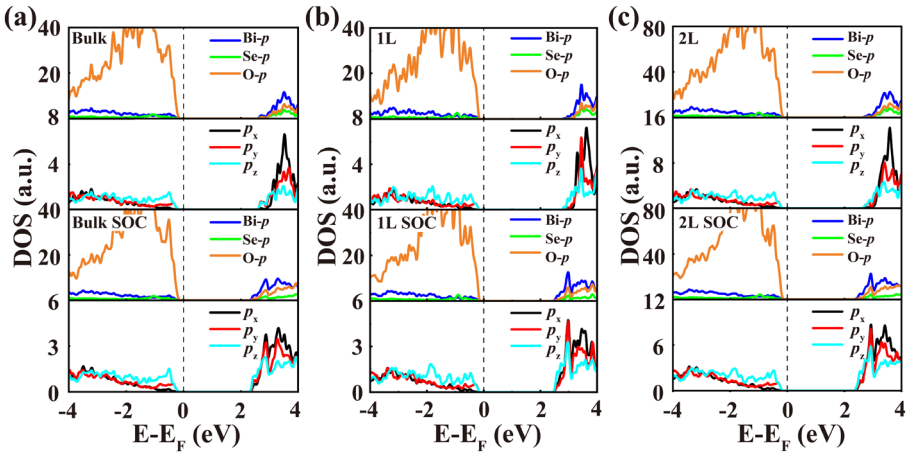

Fig. 2 (a)–(c) The LDOS and PDOS of bulk/1L/2L Bi_2SeO_5, respectively. The p orbitals of Bi, Se and O are projected in the LDOS and the p_x, p_y, and p_z orbitals of Bi are projected in the PDOS. Note that the directions of p_x, p_y, and p_z for the bulk system correspond to the *b*, *c*, and *a* directions (see Fig. 1a).

Fig. 1c and d display the band structures of 1L and 2L Bi_2SeO_5 [see 3L in Fig. S4 (ESI†)]. In the 2D limit, the initial Z point of 3D BZ folds back to the Γ point. The VBM for 1L Bi_2SeO_5 is 27.21 meV above the Γ point, which is located in the Y–Γ direction; while the CBM is much close to the Γ point, leading to an indirect bandgap of 3.06 eV [4.18 eV using the HSE06 functional (see Fig. S1b ESI†)]. When interlayer interactions are naturally included for the multilayer Bi_2SeO_5, the bandgap becomes direct and the values range from 2.91 to 2.85 eV for 2L and 3L systems (see Table 2).

To visualize the interlayer interaction, the LDOS and PDOS of 1L and 2L Bi_2SeO_5 are also calculated as shown in Fig. 2b and c. Similar to the bulk case, VBs are dominated by the O-p orbital. We also found that the Bi-p orbital has obvious contribution to CBs. For 1L Bi_2SeO_5, the p_z-orbital dominates while for 2L Bi_2SeO_5, p_z and p_y orbitals have nearly equal contributions near the CBM mimicking the bulk case. This orbital redistribution phenomenon is directly related to the interlayer interaction, which directly entangles the in-plane orbitals with the out-of-plane p_z orbital. As a result, the bonding and antibonding like charge distribution is formed and the proportion of the p_z orbital decreases near the CBM [see Fig. S2d–f (ESI†)], demonstrating the orbital mixing and redistribution.

3.1.3 SOC effect on the electronic properties. SOC is a relativistic interaction that entangles the spin and orbital degrees of freedom, and has an important effect on the electronic properties,[50,51] magnetism,[52,53] and band topology.[54,55] Considering the heavy element of Bi, one must include SOC for the electronic properties. As depicted in Fig. 1b for bulk Bi_2SeO_5, it is clearly observed that SOC can significantly reduce the bandgap from 2.79 to 2.55 eV [also see DOS in Fig. 2a-bottom]. Besides, it is observed that SOC moves the CBM slightly away from Γ to a general point along Z–R while leaves the VBM at Γ, leading to a bandgap direct-to-indirect transition. Moreover, we find that SOC only pulls down the CBs, while leaving the VBs nearly intact. This interesting behavior can be ascribed to the large/small contribution of the Bi-p orbital to CBs/VBs (see Fig. 2a).

Subsequently, we explore the SOC effect on the electronic properties of 2D Bi_2SeO_5. The results of the band structures are plotted in Fig. 1b–d. It can be seen that SOC also leads to the reduction of the bandgap. For example, the bandgap exhibits a strong layer-dependent evolution, decreasing from 3.06 to 2.73 eV for 1L Bi_2SeO_5, from 2.91 to 2.62 eV for 2L Bi_2SeO_5, and from 2.85 to 2.59 eV for 3L Bi_2SeO_5 [also see Fig. S4 (ESI†)]. In the absence of SOC, 2D Bi_2SeO_5 systems are direct bandgap semiconductors except for 1L Bi_2SeO_5. However, under the effect of SOC, the CBM is lightly shifted from Γ, and 2D Bi_2SeO_5 becomes an indirect bandgap semiconductor regardless of the layer number (see Table 2). Furthermore, as shown in Fig. 2b and c, the Bi-p orbital in 2D Bi_2SeO_5 also has a significant contribution to the CBs. Therefore, under the influence of SOC, the CBs are pulled down obviously, leading to a decrease of the bandgap.

Besides, the introduction of SOC will lead to a change in effective mass, especially the m_e since SOC mainly affects CBs, as shown in Fig. S5 (ESI†). Taking 1L Bi_2SeO_5 as an example, the magnitude of m_e is 0.447 m_0 along the Γ–X direction and 0.458 m_0 along the Γ–Y direction without the inclusion of SOC, exhibiting a relatively isotropic behavior. With SOC, m_e increases significantly along both the Γ–X and Γ–Y directions. For 2L/3L Bi_2SeO_5, when SOC is considered, the magnitude of m_e also increases along the Γ–X and Γ–Y directions. As the layer number increases from 1L to 3L Bi_2SeO_5, the in-plane anisotropy of m_e becomes more pronounced, probably due to the interlayer interaction, which mixes the in-plane and out-of-plane p orbitals. As for m_h, the impact of SOC is generally minimal [see Fig. S5b and d (ESI†)]. All results above demonstrate that SOC has a crucial influence on the electronic properties of Bi_2SeO_5.

Table 2 Lattice constants and bandgap values of bulk/2D Bi_2SeO_5

System	*a* (Å)	*b* (Å)	Bandgap (eV)	Type	Bandgap-SOC (eV)	Type
1L	16.41	5.48	3.06	Indirect	2.73	Indirect
2L	16.39	5.49	2.91	Direct	2.62	Indirect
3L	16.38	5.51	2.85	Direct	2.59	Indirect
Bulk	16.37	5.52	2.79	Direct	2.55	Indirect

With a moderate m_e, we then estimate the electrical conductivity (σ) of 1L Bi_2SeO_5 for electrons, as shown in Fig. S6 (ESI†). Due to the relaxation time approximation, we need to determine the τ of electrons. Using the DP theory, τ values are determined to be 63.56 and 114.07 fs along the x and y directions, respectively, which manifesting the strong anisotropy.[56] Therefore, σ of electron for 1L Bi_2SeO_5 is about 0.90 and 1.62 $\times$ 10^3 Ω^{-1} m^{-1} along the x and y directions with a carrier concentration of 10^{11} cm^{-2}, which are comparable to those of some 2D materials.[57,58] To demonstrate the anisotropy in 2D Bi_2SeO_5, we also estimate the τ of h along the x and y directions, which are determined to be 502.10 and 770.97 fs, respectively.

3.2 Bi_2SeO_5 based tunneling junction

After that, we turn to the transport properties of Bi_2SeO_5 based tunneling junctions because of the uniform surface of vdW layers and strong SOC.[52,59,60] The transport device model is depicted in Fig. 3a and a nonmagnetic electrode is used firstly. We calculate the transmission properties of 1L/2D Bi_2SeO_5 (details in methods), and the zero-bias transmission spectra are shown in Fig. 3b and S7a (ESI†). One can find a large transmission gap near the Fermi energy due to the bandgap of 2D Bi_2SeO_5, indicating that the transmission in this region is forbidden with zero-bias. Beyond this region, the transmission probability gradually increases. Fig. 3b and S7a (ESI†) also illustrates the impact of SOC on the transmission rate. With SOC, the scattering probability near the CBM is substantially modulated, which is consistent with the band structure (see Fig. 1). Fig. 3b and S7a (ESI†) also exhibit the trend of transmission with different thickness of scattering region. For example, stacking one more layer on single-layer Bi_2SeO_5 will obviously enhance the scattering probability, thus reducing the transmission rate. All these results suggest that SOC is also important in the Bi_2SeO_5 based tunneling junctions and thus, one can make other kinds of tunneling junctions, where SOC is crucial. Besides, Bi_2SeO_5 based tunneling junction can be fabricated in future experiments to study the layer-dependent transmission phenomenon.

Since SOC also plays a significant role in the MTJs,[61,62] we then make a device using $FeS_2/Bi_2SeO_5/FeS_2$ layers, as shown in Fig. 3c, which can be used to explore the magnetic tunneling properties. Typically, MTJs exhibit high/low conductance when two ferromagnetic electrodes have the parallel/antiparallel magnetic configurations (PC/APC), due to the relative alignment of magnetization directions. The relative difference between the PC and APC configurations can be defined as the TMR, which is calculated using the formula:

$$\mathrm{TMR} = \frac{T_{\mathrm{PC}}(E) - T_{\mathrm{APC}}(E)}{T_{\mathrm{APC}}(E)} \times 100\%, \quad (7)$$

where E represents the chemical potential, while $T_{\mathrm{PC}}(E)$ and $T_{\mathrm{APC}}(E)$ denote the transmission coefficients in the PC and APC states, respectively. As illustrated in Fig. S8 and S9 (ESI†), the k-resolved transmission coefficients for both PC and APC states of FeS_2/1L Bi_2SeO_5/FeS_2 and FeS_2/2L Bi_2SeO_5/FeS_2 MTJs are plotted, which reveal a significantly higher transmission around the Γ point and BZ boundary in the PC configuration compared to the APC state. Therefore, the calculated TMR should be positive. For 1L Bi_2SeO_5, the TMR at E = 0 eV reaches 137% (Fig. 3d), which is comparable to those of some typical vdW MTJs such as Fe_3GeTe_2/h-BN/Fe_3GeTe_2 (160%)[63] and VSe_2/CrI_3/VSe_2 (178%).[64] If chemical potential is tuned away from E = 0 eV, MTJ will exhibit a significant change in the transmission properties. For example, it shows a tremendous TMR value

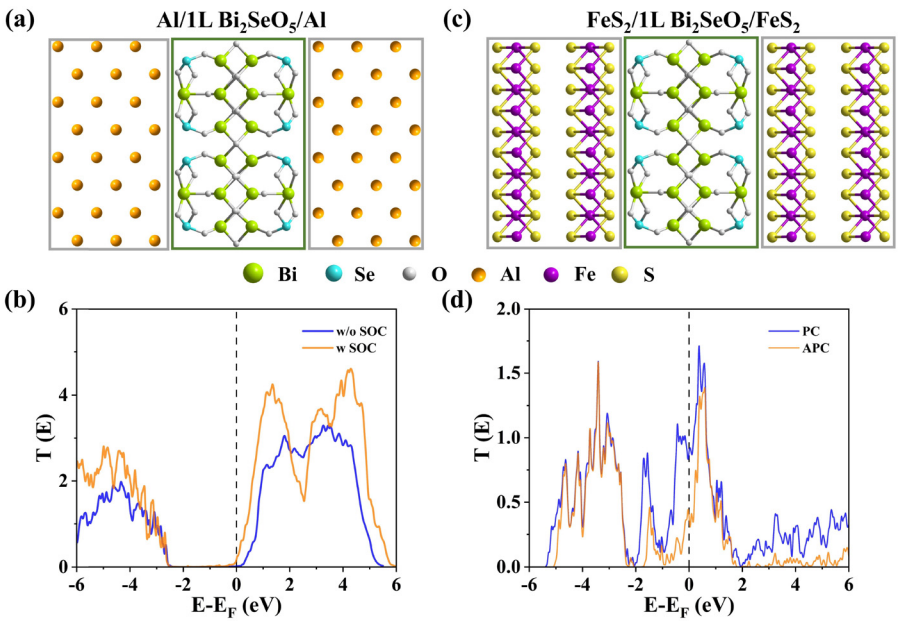

Fig. 3 (a) and (b) Schematic diagram and transmission spectra of the Al/1L Bi_2SeO_5/Al device. (c) and (d) Schematic diagram and transmission spectra of the FeS_2/1L Bi_2SeO_5/FeS_2 MTJ.

of 900% around $E = -0.26$ eV, as shown in Fig. S10a (ESI†). Similar results are observed for 2L case, as plotted in Fig. S7b and S10b (ESI†). Moreover, the TMR demonstrates a clear dependence on the layer number. For 2L Bi_2SeO_5, the TMR at $E = 0$ eV increases to 244%. Deviations in chemical potential further amplify the TMR, reaching an impressive 1800% at $E = -0.28$ eV. Therefore, Bi_2SeO_5 based vdW MTJ exhibits tremendous potential for multi-state magnetic storage in spintronics, and the layer-dependent TMR effect provides a practical strategy for optimizing the device performance.

3.3 Optical properties of bulk/2D Bi_2SeO_5

The electronic structures of bulk/2D Bi_2SeO_5, which feature a significant contribution from p-orbitals in the conduction bands of bismuth, play a crucial role in defining their distinctive optical properties. This unique electronic configuration allows for the manipulation of optical behaviors in Bi_2SeO_5, minimizing the dependence on sp-hybridization. As a result, Bi_2SeO_5 emerges as a promising candidate for both optoelectronic and electronic applications.[65] The dielectric properties of Bi_2SeO_5 have been calculated across an energy range from 0 to 12 eV.

As shown in Fig. 4a–h, the optical properties of bulk/2D Bi_2SeO_5 are essentially equivalent along the *xx* and *yy* directions. Therefore, subsequent analyses focus solely on the optical properties along the *xx* direction. The calculated spectra of $\varepsilon_1(\omega)$ are presented in Fig. 4a and the static dielectric constants, *i.e.* $\varepsilon(0)$, are provided by $\varepsilon_1(\omega)$ at $\omega = 0$. As shown in Table 3, the static dielectric constant, $\varepsilon(0)$, exhibits a dependence on the layer number. Specifically, $\varepsilon(0)$ increases monotonically with the addition of more layers while the differences between $\varepsilon(0)$ values diminish as layers are added. This behavior inversely correlates with the variation in the bandgap, a phenomenon attributed to interlayer vdW interactions.

Fig. 4a also illustrates the variation in the magnitude of the real part of dielectric function, *i.e.* $\varepsilon_1(\omega)$, as it changes with photon energy ($\hbar\omega$). When ω increases, $\varepsilon_1(\omega)$ of 1L Bi_2SeO_5 firstly increases, and reaches a peak at 3.80 eV. The peak shifts to a low energy region (red shift) and increases in magnitude with the increase of the layer number. Notably, bulk Bi_2SeO_5 exhibits a region where $\varepsilon_1(\omega)$ becomes negative. According to the wavevector equation $K = \frac{\omega}{c}\sqrt{\varepsilon(\omega)}$, $\varepsilon_1(\omega) < 0$ implies that the wavevector K becomes imaginary, indicating that light cannot propagate within this frequency range. These findings suggest that bulk Bi_2SeO_5 displays metallic characteristics under photon irradiation at these frequencies, whereas 2D Bi_2SeO_5 retains its intrinsic semiconductor properties.

$\varepsilon_2(\omega)$ of the dielectric function is closely related to the electronic band structure and reveals the absorption characteristics of materials.[66] The absorption edge of $\varepsilon_2(\omega)$ closely aligns with the bandgap values reported in Table 2, indicating the optical bandgap of Bi_2SeO_5. At this energy level, direct optical transitions occur between the highest occupied VB and the lowest unoccupied CB, attributed to interband transitions between the occupied and unoccupied states. As the energy surpasses this threshold, the curve rises sharply, indicating the presence of additional interband transitions. As illustrated in Fig. 4b, $\varepsilon_2(\omega)$ of 1L Bi_2SeO_5 increases from the edge and exhibits a prominent peak at 4.70 eV. This may correspond to the electronic transitions from the O-p orbital in VBs to the Bi-p orbital in CBs, with the magnitude of the peak being related to the maximum density of transition states. With the increase of

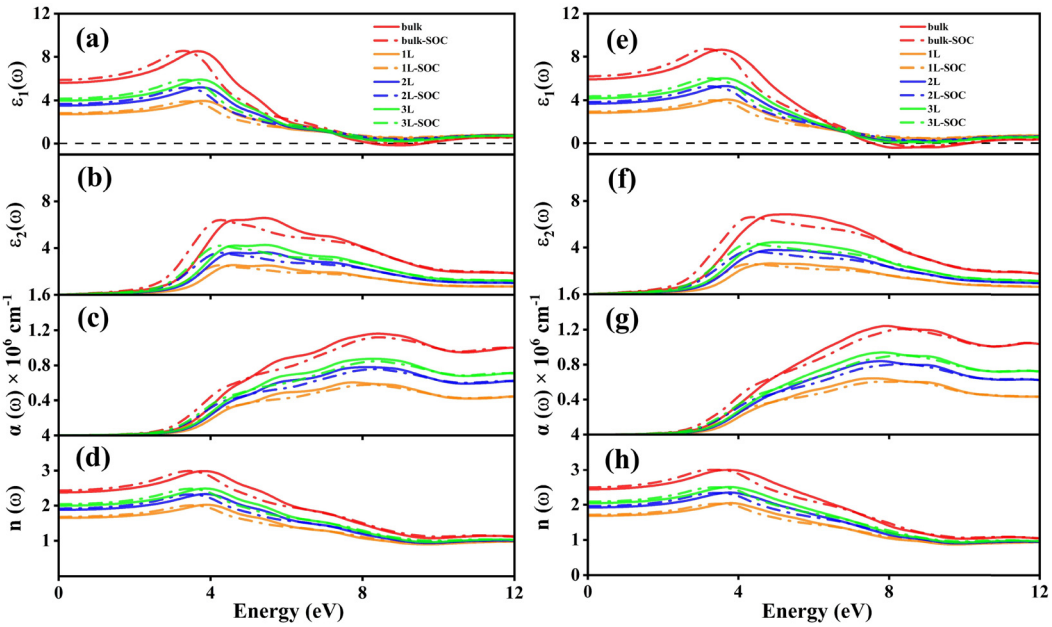

Fig. 4 (a)–(d) The real and imaginary parts of the dielectric function, as well as the absorption coefficient and refractive index, along the *xx* direction. (e)–(h) The real and imaginary parts of the dielectric function, as well as the absorption coefficient and refractive index, along the *yy* direction. We replace the unit of energy by eV, according to $E = \hbar\omega$.

Table 3 The static dielectric constants $\varepsilon(0)$, and static refractive constants $n(0)$ of bulk/2D Bi_2SeO_5

Value	1L	2L	3L	Bulk
$\varepsilon(0)$	2.69	3.50	3.96	5.62
$\varepsilon(0)$-SOC	2.82	3.65	4.16	5.90
$n(0)$	1.64	1.87	1.99	2.37
$n(0)$-SOC	1.68	1.91	2.04	2.43

the layer number, such a peak has a red shift like $\varepsilon_1(\omega)$ and shows a significant enhancement in both the visible and ultraviolet regions, as also observed in 2D MoS_2,[67] ultimately providing validation for the absorption spectra presented in Fig. 4c. The imaginary part of the dielectric function for both bulk/2D Bi_2SeO_5 consistently exhibits a peak in the ultraviolet region, which renders Bi_2SeO_5 particularly advantageous for applications in ultraviolet optoelectronic devices.

The optical absorption coefficient $\alpha(\omega)$ is crucial for assessing the ability to absorb light energy, offering valuable insights into its efficiency for solar energy conversion.[68,69] The $\alpha(\omega)$ curves are shown in Fig. 4c. One can find that $\alpha(\omega)$ of bulk/2D Bi_2SeO_5 can reach $\sim 10^6$ cm^{-1} near the visible-light range, and a significantly higher absorption is observed in the ultraviolet region, demonstrating excellent absorption properties. The increase of thickness will enhance the absorption coefficient, and the absorption peak also has a red shift, reflecting the layer dependence. These characteristics make Bi_2SeO_5 as an exceptionally competitive candidate for optoelectronic device applications.

The refractive index $n(\omega)$ quantifies the speed at which light propagates through a crystal, providing insights into the material's stability for device applications. Additionally, it can be used to determine the phase velocity of electromagnetic waves within the medium, making it a critical parameter in the study and design of optical materials.[70,71] Fig. 4d shows the refractive index of Bi_2SeO_5. The static refractive index of 1L Bi_2SeO_5 is $n(0) = 1.64$, much higher than those of other typical 2D materials such as $MgCl_2$[72] and CaF_2.[73] The static refractive indices also increase with the layer number, and the difference between the layers becomes smaller and smaller, as shown in Table 3. The $n(\omega)$ of 1L Bi_2SeO_5 increases progressively with larger photon energy, reaching a maximum value of 2.02 at 3.89 eV. As the layer number increases, the peak value of $n(\omega)$ continues to increase and undergoes a red shift, which attains a maximum value of 2.98 at 3.82 eV for bulk Bi_2SeO_5. A higher refractive index effectively focuses light, enhancing the resolution and imaging quality of optical systems. Therefore, bulk/2D Bi_2SeO_5 is well-suited for the design of high-precision optical devices.

The results presented in Fig. 4a–d and Table 3 clearly demonstrate the impact of SOC on the optical properties of Bi_2SeO_5. Under the influence of SOC, the static dielectric constant $\varepsilon(0)$ increases significantly, with the extent of this increase varying across different layer numbers. This observation indicates an enhanced SOC effect as the material's thickness increases. SOC causes both $\varepsilon_1(\omega)$ and $\varepsilon_2(\omega)$ shift to lower energy regions, accompanied by a reduction in peak values. These shifts align with the SOC-induced bandgap reduction observed in the band structure, resulting in altered interband transition energies and modified optical absorption characteristics. Similarly, in the presence of SOC, the static refractive index $n(0)$ increases, and both the $\alpha(\omega)$ and $n(\omega)$ exhibit a red shift, along with a reduction in their peak values.

3.4 Piezoelectric properties

The piezoelectricity phenomenon was firstly discovered in 1880 by Pierre *et al.*,[74] and is explained as transformation of mechanical strain and vibration energy into electrical energy. Therefore, piezoelectricity offers the opportunities for implementing renewable energy through power harvesting.[75] According to the inversion asymmetric space group *ABM*2 for bulk Bi_2SeO_5, we reasonably believe the existence of piezoelectricity in Bi_2SeO_5. By employing the first-principles-based density functional perturbation theory (DFPT), we calculate the piezoelectric stress coefficients and the calculated e_{33} component of the piezoelectric stress tensor is 0.54 C m^{-2} for bulk Bi_2SeO_5, which is comparable to those of some typical three-dimensional materials.[76,77] We also calculate the e_{11} components for 1L and 2L Bi_2SeO_5, which are 8×10^{-14} and 4×10^{-14} C m^{-1}, respectively. The piezoelectric stress coefficient of 2L is twice that of 1L Bi_2SeO_5, indicating the layer dependence and tunability.

4. Conclusions

In brief, we systematically study the layer-dependent properties of Bi_2SeO_5 through DFT calculations. 2D Bi_2SeO_5 follows the standard exponential relationship between the bandgap and the thickness. The SOC effect leads to a decrease of the bandgap and an increase of the effective mass. Importantly, the specific orbital distribution induces a significant difference of the SOC effect on VBs and CBs. Additionally, the vdW MTJ based on $FeS_2/Bi_2SeO_5/FeS_2$ exhibits strong TMR, which can be tuned to $\sim$1800%. The optical properties of 2D Bi_2SeO_5 are explored, which show an obvious red shift as the layer number increases. The computed piezoelectric coefficient also shows the layer dependence. Overall, vdW Bi_2SeO_5 provides a superior opportunity for new electronic and optical device applications.

Data availability

The data that support the findings of this study are available from the corresponding author, [Chenqiang Hua], upon reasonable request.

Conflicts of interest

There are no conflicts to declare.

Acknowledgements

The authors thank Shengyuan A. Yang (from University of Macau) and Shenbo Yang (from HZWTECH) for help and

discussions regarding this study. The authors acknowledge financial support from the Natural Science Foundation of Zhejiang Province (No. LY23E020010 and Q23A040023), the National Natural Science Foundation of China (Grants No. 12204029), and the funding of ''Leading Innovative and Entrepreneur Team Introduction Program of Zhejiang'' (Grant No. 2020R01002). Yao Wang acknowledges the funding from China Postdoctoral Science Foundation (2023M743098). Chenqiang Hua acknowledges the start-up funding from Hangzhou International Innovation Institute of Beihang University (Grant No. 2024KQ009).

References

1 K. W. Plumb, J. P. Clancy, L. J. Sandilands, V. V. Shankar, Y. F. Hu, K. S. Burch, H.-Y. Kee and Y.-J. Kim, *Phys. Rev. B*, 2014, **90**, 041112.
2 Z. Wang, D. K. Ki, H. Chen, H. Berger, A. H. MacDonald and A. F. Morpurgo, *Nat. Commun.*, 2015, **6**, 8339.
3 H. Weng, C. Fang, Z. Fang, B. A. Bernevig and X. Dai, *Phys. Rev. X*, 2015, **5**, 011029.
4 W. Xiong, C. Xia, Y. Peng, J. Du, A. Stroppa and W. Ren, *Phys. Chem. Chem. Phys.*, 2016, **18**, 6534–6540.
5 T. Hu, F. Jia, G. Zhao, J. Wu, A. Stroppa and W. Ren, *Phys. Rev. B*, 2018, **97**, 235404.
6 M. Gmitra, D. Kochan and J. Fabian, *Phys. Rev. Lett.*, 2013, **110**, 246602.
7 D. Santos-Cottin, M. Casula, G. Lantz, Y. Klein, L. Petaccia, P. Le Fèvre, F. Bertran, E. Papalazarou, M. Marsi and A. Gauzzi, *Nat. Commun.*, 2016, **7**, 11258.
8 N. Lanatà, Y.-X. Yao, C.-Z. Wang, K.-M. Ho, J. Schmalian, K. Haule and G. Kotliar, *Phys. Rev. Lett.*, 2013, **111**, 196801.
9 L. Lang, J.-H. Yang, H.-R. Liu, H. J. Xiang and X. G. Gong, *Phys. Lett. A*, 2014, **378**, 290–293.
10 T.-A. Chen, C.-P. Chuu, C.-C. Tseng, C.-K. Wen, H. S. P. Wong, S. Pan, R. Li, T.-A. Chao, W.-C. Chueh, Y. Zhang, Q. Fu, B. I. Yakobson, W.-H. Chang and L.-J. Li, *Nature*, 2020, **579**, 219–223.
11 C. R. Dean, A. F. Young, I. Meric, C. Lee, L. Wang, S. Sorgenfrei, K. Watanabe, T. Taniguchi, P. Kim, K. L. Shepard and J. Hone, *Nat. Nanotechnol.*, 2010, **5**, 722–726.
12 T. Knobloch, Y. Y. Illarionov, F. Ducry, C. Schleich, S. Wachter, K. Watanabe, T. Taniguchi, T. Mueller, M. Waltl, M. Lanza, M. I. Vexler, M. Luisier and T. Grasser, *Nat. Electron.*, 2021, **4**, 98–108.
13 J. S. Lee, S. H. Choi, S. J. Yun, Y. I. Kim, S. Boandoh, J. H. Park, B. G. Shin, H. Ko, S. H. Lee, Y. M. Kim, Y. H. Lee, K. K. Kim and S. M. Kim, *Science*, 2018, **362**, 817–821.
14 J. Xue, J. Sanchez-Yamagishi, D. Bulmash, P. Jacquod, A. Deshpande, K. Watanabe, T. Taniguchi, P. Jarillo-Herrero and B. J. LeRoy, *Nat. Mater.*, 2011, **10**, 282–285.
15 T. Ando, A. B. Fowler and F. Stern, *Rev. Mod. Phys.*, 1982, **54**, 437–672.
16 Z. Ye, T. Cao, K. O'Brien, H. Zhu, X. Yin, Y. Wang, S. G. Louie and X. Zhang, *Nature*, 2014, **513**, 214–218.
17 R. Fei, W. Kang and L. Yang, *Phys. Rev. Lett.*, 2016, **117**, 097601.
18 Y. Cao, V. Fatemi, A. Demir, S. Fang, S. L. Tomarken, J. Y. Luo, J. D. Sanchez-Yamagishi, K. Watanabe, T. Taniguchi, E. Kaxiras, R. C. Ashoori and P. Jarillo-Herrero, *Nature*, 2018, **556**, 80–84.
19 T. Li, T. Tu, Y. Sun, H. Fu, J. Yu, L. Xing, Z. Wang, H. Wang, R. Jia, J. Wu, C. Tan, Y. Liang, Y. Zhang, C. Zhang, Y. Dai, C. Qiu, M. Li, R. Huang, L. Jiao, K. Lai, B. Yan, P. Gao and H. Peng, *Nat. Electron.*, 2020, **3**, 473–478.
20 C. Tan, M. Yu, J. Tang, X. Gao, Y. Yin, Y. Zhang, J. Wang, X. Gao, C. Zhang, X. Zhou, L. Zheng, H. Liu, K. Jiang, F. Ding and H. Peng, *Nature*, 2023, **616**, 66–72.
21 C. Zhang, T. Tu, J. Wang, Y. Zhu, C. Tan, L. Chen, M. Wu, R. Zhu, Y. Liu, H. Fu, J. Yu, Y. Zhang, X. Cong, X. Zhou, J. Zhao, T. Li, Z. Liao, X. Wu, K. Lai, B. Yan, P. Gao, Q. Huang, H. Xu, H. Hu, H. Liu, J. Yin and H. Peng, *Nat. Mater.*, 2023, **22**, 832–837.
22 J.-K. Huang, Y. Wan, J. Shi, J. Zhang, Z. Wang, W. Wang, N. Yang, Y. Liu, C.-H. Lin, X. Guan, L. Hu, Z.-L. Yang, B.-C. Huang, Y.-P. Chiu, J. Yang, V. Tung, D. Wang, K. Kalantar-Zadeh, T. Wu, X. Zu, L. Qiao, L.-J. Li and S. Li, *Nature*, 2022, **605**, 262–267.
23 P. E. Blöchl, *Phys. Rev. B: Condens. Matter Mater. Phys.*, 1994, **50**, 17953–17979.
24 G. Kresse and J. Furthmüller, *Phys. Rev. B: Condens. Matter Mater. Phys.*, 1996, **54**, 11169–11186.
25 J. P. Perdew, K. Burke and M. Ernzerhof, *Phys. Rev. Lett.*, 1996, **77**, 3865–3868.
26 J. Klimeš, D. R. Bowler and A. Michaelides, *Phys. Rev. B: Condens. Matter Mater. Phys.*, 2011, **83**, 195131.
27 Y. Zhai, S. Baniya, C. Zhang, J. Li, P. Haney, C.-X. Sheng, E. Ehrenfreund and Z. V. Vardeny, *Sci. Adv.*, 2017, **3**, e1700704.
28 J. Heyd, G. E. Scuseria and M. Ernzerhof, *J. Chem. Phys.*, 2003, **118**, 8207–8215.
29 C. Hua, F. Sheng, Q. Hu, Z.-A. Xu, Y. Lu and Y. Zheng, *J. Phys. Chem. Lett.*, 2018, **9**, 6695–6701.
30 J. Qiao, X. Kong, Z.-X. Hu, F. Yang and W. Ji, *Nat. Commun.*, 2014, **5**, 4475.
31 J. Taylor, H. Guo and J. Wang, *Phys. Rev. B: Condens. Matter Mater. Phys.*, 2001, **63**, 245407.
32 M. Brandbyge, J. L. Mozos, P. Ordejón, J. Taylor and K. Stokbro, *Phys. Rev. B: Condens. Matter Mater. Phys.*, 2002, **65**, 2469–9950.
33 J. M. Soler, E. Artacho, J. D. Gale, A. García, J. Junquera, P. Ordejón and D. Sánchez-Portal, *J. Phys.: Condens. Matter*, 2002, **14**, 2745–2779.
34 O. Rademacher, H. Göbel, M. Ruck and H. Oppermann, *Z. Kristallogr. – New Cryst. Struct.*, 2001, **216**, 29–30.
35 S. Grimme, S. Ehrlich and L. Goerigk, *J. Comput. Chem.*, 2011, **32**, 1456–1465.
36 S. N. Steinmann and C. Corminboeuf, *J. Chem. Phys.*, 2011, **134**, 044117.
37 S. N. Steinmann and C. Corminboeuf, *J. Chem. Theory Comput.*, 2011, **7**, 3567–3577.
38 J. Klimeš, D. R. Bowler and A. Michaelides, *J. Phys.: Condens. Matter*, 2010, **22**, 022201.

39 I. Hamada, *Phys. Rev. B: Condens. Matter Mater. Phys.*, 2014, **89**, 121103.
40 J. Shi, J. Zhang, L. Yang, M. Qu, D.-C. Qi and K. H. L. Zhang, *Adv. Mater.*, 2021, **33**, 2006230.
41 L.-H. Zeng, S.-H. Lin, Z.-J. Li, Z.-X. Zhang, T.-F. Zhang, C. Xie, C.-H. Mak, Y. Chai, S. P. Lau, L.-B. Luo and Y. H. Tsang, *Adv. Funct. Mater.*, 2018, **28**, 1705970.
42 K. Kaasbjerg, K. S. Thygesen and K. W. Jacobsen, *Phys. Rev. B: Condens. Matter Mater. Phys.*, 2012, **85**, 115317.
43 S. Bruzzone and G. Fiori, *Appl. Phys. Lett.*, 2011, **99**, 222108.
44 Z. Liang, J. Zhang, C. Hua, Y. Wang and F. Song, *Phys. Rev. B*, 2024, **110**, 085110.
45 T. Björkman, A. Gulans, A. V. Krasheninnikov and R. M. Nieminen, *Phys. Rev. Lett.*, 2012, **108**, 235502.
46 J. H. Jung, C.-H. Park and J. Ihm, *Nano Lett.*, 2018, **18**, 2759–2765.
47 B. Liu, X. Jia, Y. Nie and H. Ye, *Appl. Surf. Sci.*, 2022, **572**, 151485.
48 S. Tongay, J. Zhou, C. Ataca, K. Lo, T. S. Matthews, J. Li, J. C. Grossman and J. Wu, *Nano Lett.*, 2012, **12**, 5576–5580.
49 W. S. Yun, S. W. Han, S. C. Hong, I. G. Kim and J. D. Lee, *Phys. Rev. B: Condens. Matter Mater. Phys.*, 2012, **85**, 033305.
50 D. Ram, J. Singh, S. Banerjee, A. Sundaresan, D. Samal, V. Kanchana and Z. Hossain, *Phys. Rev. B*, 2024, **109**, 155152.
51 S. Chakraborty and S. Raj, *Phys. Rev. B*, 2023, **107**, 035420.
52 M. Zhang, Q. Hu, Y. Huang, C. Hua, M. Cheng, Z. Liu, S. Song, F. Wang, H. Lu, P. He, G.-H. Cao, Z.-A. Xu, Y. Lu, J. Yang and Y. Zheng, *Small*, 2023, **19**, 2300964.
53 J. Zhang, Y. Wang, C. Hua, S. Yang, Y. Liu, J. Luo, T. Liu, J. Nai and X. Tao, *Phys. Rev. B*, 2022, **106**, 235401.
54 Z. Huang, Z. Zhang and P. Cui, *Phys. Rev. B*, 2024, **109**, 224516.
55 Y. Yang, H. Xing, G. Tang, C. Hua, C. Yao, X. Yan, Y. Lu, J. Hu, Z. Mao and Y. Liu, *Phys. Rev. B*, 2021, **103**, 125160.
56 W. Yi, X. Chen, Z. Wang, Y. Ding, B. Yang and X. Liu, *J. Mater. Chem. C*, 2019, **7**, 7352–7359.
57 D. Qin, P. Yan, G. Ding, X. Ge, H. Song and G. Gao, *Sci. Rep.*, 2018, **8**, 2764.
58 J. Xiang, B. Dai, X.-W. Zhang, H.-Z. Guo, W.-L. Cheng and N.-N. Ge, *Mater. Today Commun.*, 2022, **33**, 104789.
59 Y. Zhu, X. Y. Guo, L. N. Jiang, Z. R. Yan, Y. Yan and X. F. Han, *Phys. Rev. B*, 2021, **103**, 134437.
60 J. Yang, S. Fang, Y. Peng, S. Liu, B. Wu, R. Quhe, S. Ding, C. Yang, J. Ma, B. Shi, L. Xu, X. Sun, G. Tian, C. Wang, J. Shi, J. Lu and J. Yang, *Phys. Rev. Appl.*, 2021, **16**, 024011.
61 E. Elahi, M. A. Khan, M. Suleman, A. Dahshan, S. Rehman, H. M. Waseem Khalil, M. A. Rehman, A. M. Hassan, G. Koyyada, J. H. Kim and M. F. Khan, *Mater. Today*, 2024, **72**, 183–206.
62 J.-I. Inoue, M. Tsujikawa and M. Shirai, *Phys. Rev. B*, 2023, **108**, 014431.
63 Z. Wang, D. Sapkota, T. Taniguchi, K. Watanabe, D. Mandrus and A. F. Morpurgo, *Nano Lett.*, 2018, **18**, 4303–4308.
64 F. Li, B. Yang, Y. Zhu, X. Han and Y. Yan, *Appl. Surf. Sci.*, 2020, **505**, 144648.
65 H. Bu, H. Zheng, H. Zhang, H. Yuan and J. Zhao, *Sci. Rep.*, 2020, **10**, 6808.
66 L.-K. Gao, Y.-L. Tang and X.-F. Diao, *Appl. Sci.*, 2020, **10**, 5055.
67 A. Kumar and P. K. Ahluwalia, *Mater. Chem. Phys.*, 2012, **135**, 755–761.
68 H. Ahmed, S. Mukhtar, S. Agathopoulos and S. Z. Ilyas, *Phys. B*, 2022, **640**, 414085.
69 A. Soni, V. Gupta, C. M. Arora, A. Dashora and B. L. Ahuja, *Sol. Energy*, 2010, **84**, 1481–1489.
70 A. Benghia, T. Dahame and B. Bentria, *Opt. Mater.*, 2016, **54**, 269–275.
71 G. Nazir, A. Ahmad, M. F. Khan and S. Tariq, *Comput. Condens. Matter*, 2015, **4**, 32–39.
72 H. R. Mahida, A. Patel, D. Singh, Y. Sonvane, P. B. Thakor and R. Ahuja, *Superlattices Microstruct.*, 2022, **162**, 107132.
73 H. Alavi-Rad and S. B. Touski, *Phys. B*, 2024, **676**, 415650.
74 P. Zubko, G. Catalan and A. K. Tagantsev, *Annu. Rev. Mater. Sci.*, 2013, **43**, 387–421.
75 Q. Deng, M. Kammoun, A. Erturk and P. Sharma, *Int. J. Solids Struct.*, 2014, **51**, 3218–3225.
76 H. Wang, S. Sun, L. Kong, W. Zhang, Y. Bai and M. Feng, *J. Mater. Sci.*, 2021, **56**, 15898–15905.
77 K. Choudhary, K. F. Garrity, V. Sharma, A. J. Biacchi, A. R. Hight Walker and F. Tavazza, *npj Comput. Mater.*, 2020, **6**, 64.